

Single-molecule nucleic acid interactions monitored on a label-free microcavity biosensor platform

Martin D. Baaske, Matthew R. Foreman and Frank Vollmer

SUPPLEMENTARY INFORMATION 1. NEAR FIELD ENHANCEMENTS

In this section we detail finite element simulations of gold nanorods positioned in close proximity to a dielectric microsphere immersed in an aqueous environment. Supplementary Table 1 lists a number of the associated simulation parameters. The approach we adopt is similar to that first proposed by Kaplan et al. [1] for a microtoroid geometry, however, here we make suitable adaptations such that microsphere resonators can be considered. In short, by exploiting symmetry considerations and *a priori* knowledge of whispering gallery mode profiles, a reduced simulation volume is defined from which the associated eigenmodes are found using the COMSOL Multiphysics (v4.3a) eigensolver.

1. Simulation geometry

In a biosensing context, realistic microspheres typically have a radius of a few tens of microns. Such a large size proves prohibitive for finite element analysis, since the associated

Parameter Name	Value
Microsphere radius, a	30 μm
Microsphere refractive index, n_r	1.45367
Unperturbed WGM wavelength, λ_0	780.911 nm
Unperturbed WGM polarisation	TE
Unperturbed WGM Q factor	7.66×10^5
WGM mode index, l	340
Host (water) refractive index, n_h	$1.32979 + i 1.395 \times 10^{-7}$
Nanoparticle-surface distance, d	7 nm
Nanorod diameter D	12 nm
Nanorod aspect ratio L/D	3.5
Gold refractive index n_p	Palik [2]
Polar slice angle	10°

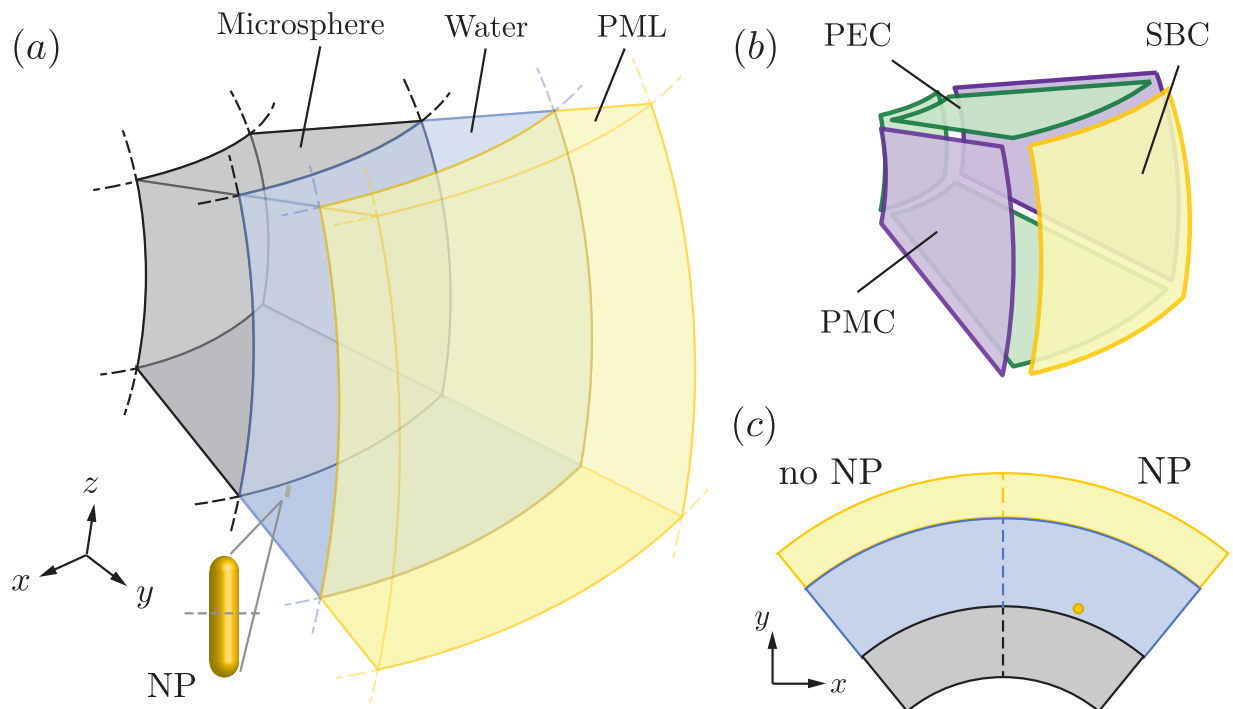
Supplementary Table 1. Assorted simulation parameters used in calculation of near field enhancement factors.

simulation domain is too large for standard desktop computers. Importantly, however, a number of observations allows the simulation domain to be greatly reduced to a more tractable size.

Firstly, it is noted, that we are only interested in the study of whispering gallery modes (WGMs) supported within a microsphere. Given the bound nature of these modes, the majority of the mode energy is concentrated near the surface of the microsphere, such that the centermost region of the microsphere interior is of little interest. Likewise, the evanescent field penetrates only a short distance into the host medium, such that only a small region of the exterior need be considered. Similarly, for fundamental WGMs, as principally used in sensing applications, modes are confined to lie in (or near) the equatorial plane of the microsphere, allowing further reductions.

Secondly, the symmetry of the WGMs allows further reductions in simulation volume. For an unperturbed whispering gallery mode of order l , a strong degree of rotational symmetry about the polar axis is present. Consequently, simulation of the full 2π range of the azimuthal angle is not required. Instead, an angular slice need only be considered, with appropriate boundary conditions chosen (discussed below) to replicate the full nature of the whispering gallery mode. In the presence of a nanoparticle (NP), however, the situation requires additional thought, since the presence of the nanoparticle disturbs the mode and breaks the azimuthal symmetry. Crucially, the interaction between the nanoparticle is perturbative in nature, such that the mode regenerates quickly as you move further from the position of the nanoparticle, in turn meaning only a small segment of the sphere need be considered as for the unperturbed case. In so doing it is vital to ensure the angular slice is wide enough to ensure the nanoparticle has negligible effect at the boundaries, as discussed more fully in the work of Kaplan et al. [1]. Given these observations the simulation domain can be reduced from a full spherical volume, to that of a tesseroid as shown in Supplementary Figure 1.

Simulation errors introduced by using this tesseroidal domain can be reduced to below that of the inherent numerical error (e.g. through finite discretisation of the simulation volume), if the simulation is setup correctly. Selection of the appropriate boundary conditions and geometrical parameters are hence important in simulations, so as to ensure that the reduced simulation domain accurately reflects the full physical system as closely as possible. We thus detail appropriate choices here. It should be noted that simulations were per-



Supplementary Figure 1. (a) Schematic of the reduced tesseroidal simulation volume showing the division into distinct domains for the microsphere, host medium, perfectly matched layer and nanoparticle. (b) Boundary conditions for external faces of the simulation volume. (c) Cross-section of equatorial plane of simulation volume, showing regions with and without a nanoparticle.

formed using the commercial COMSOL Multiphysics v4.3a software package (in particular the RF module eigensolver), such that here we adopt the parlance matching that found in the COMSOL documentation.

WGM resonators are inherently lossy, with energy escaping, for example, via radiation losses from the resonator. To account for such losses in our simulations a perfectly matched layer (PML) [3] is introduced at the outer face of the tesseroid (see Supplementary Figure 1), with an external scattering boundary condition (SBC). Presence of the PML, moreover, allows the Q factor of each eigenmode to be extracted, which can be used to help verify correct operation of the simulation by comparison to solution of the exact resonance condition [4], and to allow easy identification of WGMs from the myriad of eigenmodes output by the COMSOL eigensolver. When considering the azimuthal faces of the tesseroidal volume, we recall, that we wish to simulate a rotationally symmetric scenario. Accordingly we may

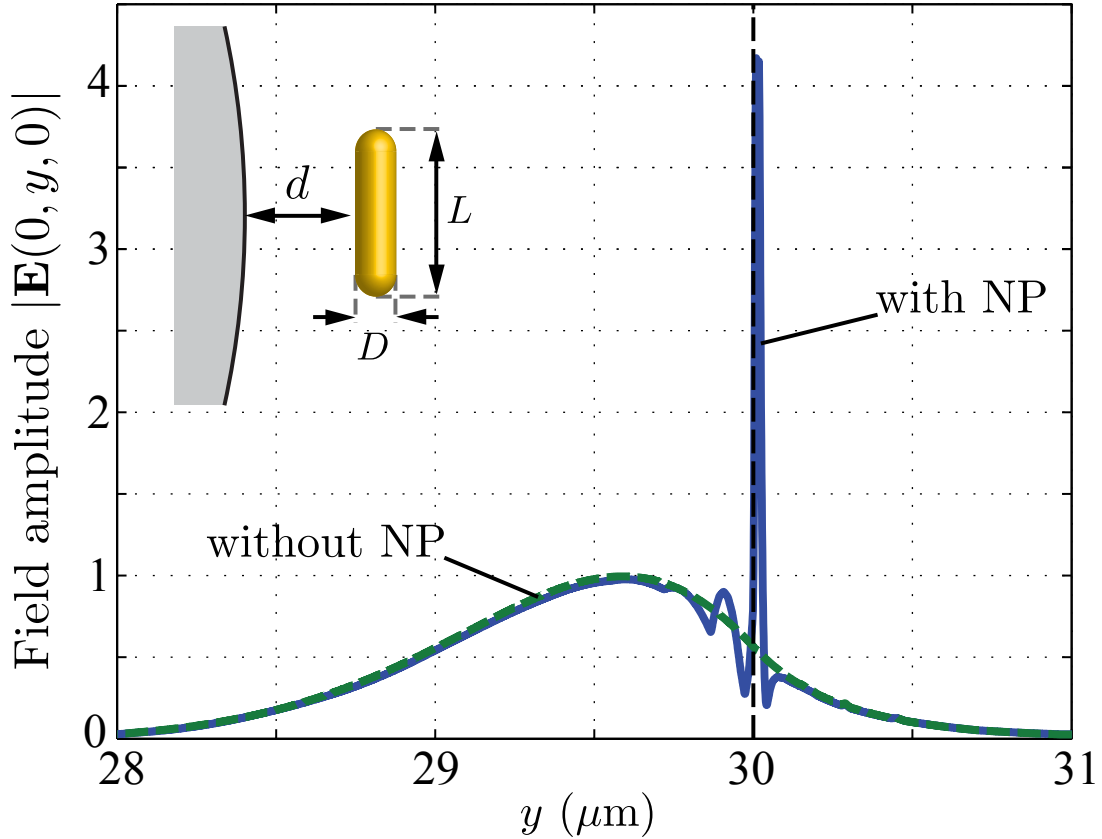
choose to select either a perfect electric conductor (PEC) or perfect magnetic conductor (PMC) boundary condition for the azimuthal faces (Supplementary Figure 1(b)). So doing, has the effect of mirroring the simulated volume. For physically meaningful results, therefore, the boundaries should be placed at the nodes (PEC) or anti-nodes (PMC) of the WGM. We elect to use the latter. Furthermore, note that the angular opening in both the azimuthal and polar directions should be an integer fraction of the full 2π rotation. Additionally, given output modes from the COMSOL eigensolver are only meaningful in a relative sense for a single mode (i.e. absolute values between different simulations can not be directly compared) due to the normalisation methods used in COMSOL, a segment with and without a NP must be considered in a single simulation as depicted in Supplementary Figure 1(c). All remaining boundaries are then set to PECs since the field on these boundaries are negligible by construction.

The NP considered in our simulations was a gold nanorod, modeled as a prolate circular cylinder with hemispherical end caps as shown in Supplementary Figures 1 and 2. To maximise coupling with the WGM, the NP was aligned parallel to the unperturbed WGM field at the position of the NP, which for a TE mode implies the long axis of the NP is perpendicular to the equatorial plane. Given the symmetry of this arrangement a PEC boundary bisecting the NP, as depicted in Supplementary Figure 1(a), can also be introduced.

2. Material properties, meshing and solver properties

Throughout all simulations a $30\ \mu\text{m}$ radius microsphere was taken and assumed to be made from fused silica with a refractive index of 1.45367 and immersed in water with a refractive index of $1.32979 + i 1.395 \times 10^{-7}$ (as found by interpolation of data from Hale and Query [5]). For a $30\ \mu\text{m}$ radius microsphere radiation losses are dominant, however we include water absorption for completeness. Finally the NP was assumed to be made of gold, with refractive index data interpolated from that of Palik [2]. To include material dispersion in the COMSOL simulations correctly, it was necessary to define a second electric wave equation node to the solver configuration so as to override the material properties within the domain of the NP, to those defined by the appropriate interpolation functions.

With regards to meshing, a swept mesh was used to discretise the domain of the microsphere and within the PML. Other domains were meshed using a free tetrahedral discreti-

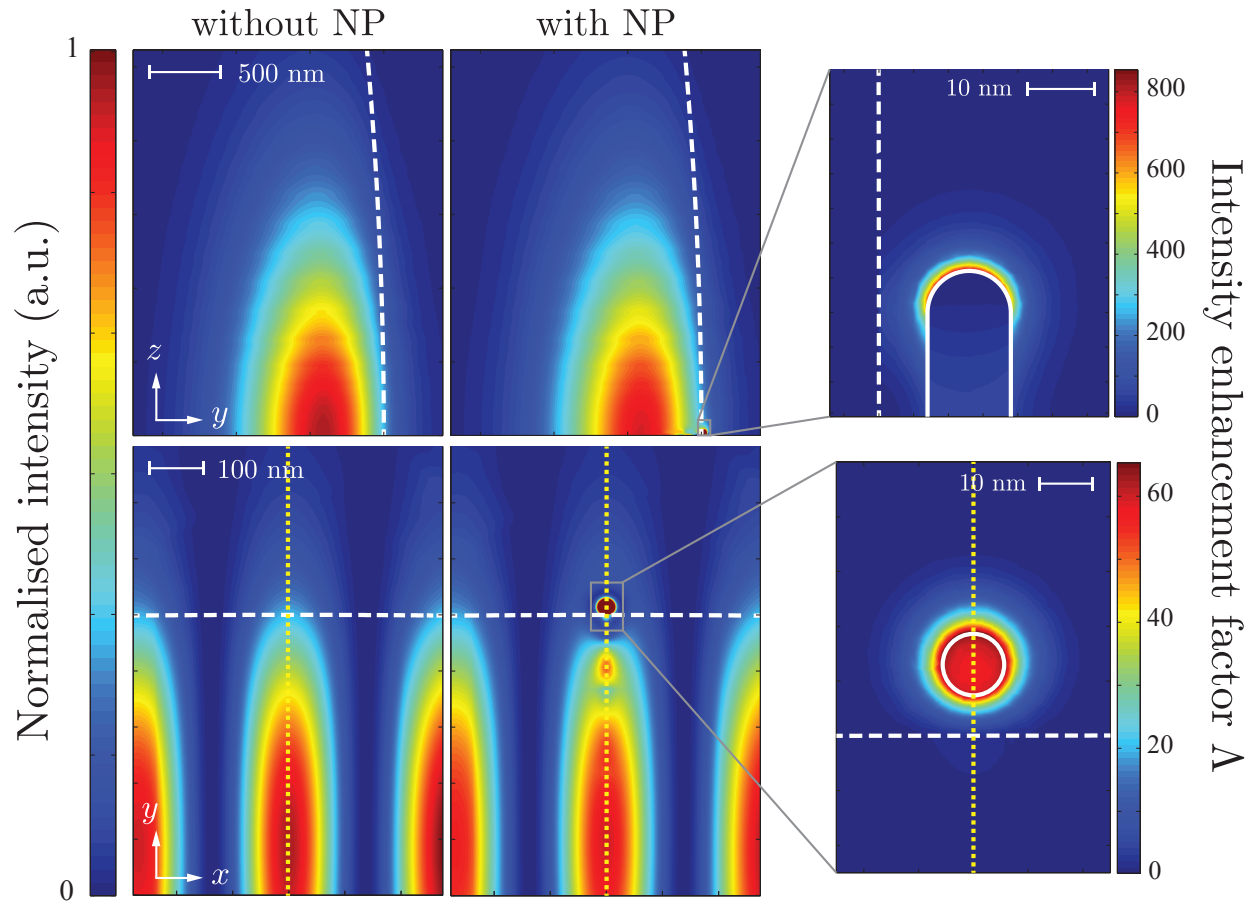


Supplementary Figure 2. Line profiles of unperturbed (dashed green) and perturbed (solid blue) $l = 340$ TE whispering gallery mode field distribution for a $30 \mu\text{m}$ radius microsphere. Line profiles were taken along the yellow dashed line shown in Supplementary Figure 3. Field amplitude is plotted to improve visibility of the unperturbed mode.

sation. Conversion between meshes was performed on adjoining interfaces by insertion of diagonal edges. Finer meshes were used in the vicinity of the NP to allow greater spatial resolution in the resulting fields. The nanorod was placed a distance of 7 nm from the microsphere surface to mitigate meshing problems.

3. Results

To verify correct operation of finite element simulations an unperturbed fundamental whispering gallery mode was found (i.e. the eigenmode found without a NP present) and characterised. Cross-sections of the $l = 340$ TE mode considered can be seen in Supplemen-



Supplementary Figure 3. Polar yz - (top) and equatorial xy - (bottom) cross-sections of the intensity distributions of an unperturbed (left) and perturbed (middle) whispering gallery mode. Intensity distributions have been normalised to the peak modal intensity for the unperturbed case. Note that color scales have been limited to range from zero to unity, to emphasise the perturbation to the mode distribution. Intensity distributions hence appear saturated near the nanoparticle. Strong intensity enhancements (right) are however seen in the close vicinity of the nanoparticle. In all panels white dashed (solid) lines denote the microsphere (nanorod) surface. Yellow dotted lines correspond to line profiles shown in Supplementary Figure 2.

tary Figure 3. The resonance wavelength and associated Q factor were determined to be 782.038 nm and 7.20×10^5 respectively compared with the theoretical values of 780.911 nm and 7.663×10^5 . Upon introduction of the nanorod, the whispering gallery mode distribution is perturbed locally, with strong near fields seen in the vicinity of the nanorod (see Supplementary Figure 3). Near field intensity enhancements are maximal at the ends of

the nanorod with enhancements of over 800 seen for $L/D = 3.5$, however strong enhancements of ~ 60 are also seen at more central regions of the rod. It is noted that the latter figure is comparable to that achievable with near-resonance a nano-shell particle geometry [6]. In addition to the distributions shown in Supplementary Figure 3, line profiles of the unperturbed and perturbed modes along the direction joining the microsphere and nanorod centers are shown in Supplementary Figure 2. For clarity Supplementary Figure 2 plots field amplitude as opposed to intensity, however, clear enhancements are seen. Noting the peak amplitude in the presence of the NP is ~ 4 , as compared to the amplitude at the same position without the NP of ~ 0.25 , the maximum intensity enhancement is ~ 64 as corresponds to those shown in Supplementary Figure 3.

SUPPLEMENTARY INFORMATION 2. NANOPARTICLE AND DNA INDUCED RESONANCE SHIFTS

1. Background theory

In this section we consider the effect of binding of a NP or DNA molecule to a WGM resonator. We consider a spherical WGM resonator with electric permittivity ϵ_r immersed in a host medium of electric permittivity ϵ_h and assume the NP can be described by the permittivity tensor $\overleftrightarrow{\epsilon}_p(\mathbf{r})$ which in general can depend on spatial position e.g. for composite nanoshell particles. It should be noted that for generality we allow the NP to possess a non-scalar permittivity as is applicable to anisotropic NPs.

Reactive resonance shifts in WGMRs have been extensively studied in the literature and have been derived using both a perturbation based approach as well as more rigorous Mie scattering calculations [6, 7]. For simplicity, in this work we shall consider the first order perturbation result [7] whereby it was shown that the change, $\Delta\omega$ in WGM resonance frequency, ω , is given by (with appropriate generalisation to allow for anisotropic NPs)

$$\frac{\Delta\omega}{\omega} \approx -\frac{1}{2} \frac{\int_{V_p} \mathbf{E}^\dagger(\mathbf{r}) \left[\overleftrightarrow{\epsilon}_p(\mathbf{r}) - \epsilon_h \overleftrightarrow{I} \right] \mathbf{E}'(\mathbf{r}) d\mathbf{r}}{\int_V \epsilon(\mathbf{r}) |\mathbf{E}(\mathbf{r})|^2 d\mathbf{r}} = -\frac{1}{2} \frac{\Delta U}{U}, \quad (1)$$

where \overleftrightarrow{I} is the 3×3 identity matrix, \dagger denotes the Hermitian adjoint, V_p (V) denotes the volume of the NP (all space), \mathbf{E} (\mathbf{E}') denotes the unperturbed (perturbed) mode distribution respectively and $\epsilon(\mathbf{r})$ is the permittivity distribution before introduction of the NP, such that

$\epsilon(\mathbf{r}) = \epsilon_r$ for \mathbf{r} within the WGMR and ϵ_h otherwise. In the derivation of Teraoka and Arnold [7] permittivities were assumed to be real, such that the resonance frequency ω in Eq. (1) was real. It can, however, be shown that Eq. (1) is applicable for absorbing media (with complex ϵ) if $\omega = \omega_0 - i\gamma_0/2$ is taken as a complex resonance frequency, with the real (imaginary) part defining the resonance frequency (linewidth). We note that γ_0 can account for all losses mechanisms in the bare cavity, such as radiation (curvature) losses, absorption and surface scattering. The shift of the (real) resonance frequency then quickly follows and is given by

$$\frac{\Delta\omega_0}{\omega_0} \approx -\frac{1}{2} \left(\text{Re} \left[\frac{\Delta U}{U} \right] + \frac{1}{2Q_0} \text{Im} \left[\frac{\Delta U}{U} \right] \right), \quad (2)$$

where for high Q resonances $Q_0 = \omega_0/\gamma_0$ is the quality factor the WGM resonance, whilst

$$\frac{\Delta\gamma_{\text{abs}}}{\omega_0} \approx \left(\text{Im} \left[\frac{\Delta U}{U} \right] - \frac{1}{2Q_0} \text{Re} \left[\frac{\Delta U}{U} \right] \right). \quad (3)$$

This latter equation describes the additional broadening of the WGM due to the presence of an absorbing NP (hence motivating the choice of subscript), as can be seen by noting that $\Delta\gamma_{\text{abs}} \rightarrow 0$ as $\text{Im}[\overset{\leftrightarrow}{\epsilon}_p] \rightarrow 0$. We note that for high Q WGMRs the second term in both Eqs. (2) and (3) can usually safely be ignored, as will be done henceforth. We will also henceforth assume, for simplicity that ϵ_h and $\epsilon_r \in \mathbb{R}$, for the purposes of calculating perturbative shifts and broadening, however we note that the effect of absorption on the natural resonance linewidth can (and should) be included within γ_0 . In contrast, no such restriction is made for the permittivity of the NP, $\overset{\leftrightarrow}{\epsilon}_p(\mathbf{r})$, since we seek to describe interaction of the WGM with metallic NPs.

To determine the frequency shift $\Delta\omega$ we note that application of an electric field on an NP induces an additional material polarisation $\mathbf{P}(\mathbf{r}) = \epsilon_0(\overset{\leftrightarrow}{\epsilon}_p - \epsilon_h \overset{\leftrightarrow}{I})\mathbf{E}(\mathbf{r})$, within the particle volume. Since $\epsilon_0 \overset{\leftrightarrow}{\epsilon}_p \mathbf{E}'(\mathbf{r}) = \epsilon_0 \epsilon_h \mathbf{E}(\mathbf{r}) + \mathbf{P}(\mathbf{r})$ Eq. (2) can be written in the form:

$$\frac{\Delta\omega_0}{\omega_0} \approx -\frac{1}{2} \text{Re} \left[\frac{\int_{V_p} \mathbf{E}^\dagger(\mathbf{r}) \mathbf{P}(\mathbf{r}) d\mathbf{r}}{\int_V \epsilon_0 \epsilon(\mathbf{r}) |\mathbf{E}(\mathbf{r})|^2 d\mathbf{r}} \right]. \quad (4)$$

Following [8] this can be rewritten as:

$$\frac{\Delta\omega}{\omega_0} = -\frac{1}{4} \epsilon_0 \epsilon_h \frac{\text{Re}[\mathbf{E}^\dagger(\mathbf{r}_p) \overset{\leftrightarrow}{\alpha} \mathbf{E}(\mathbf{r}_p)]}{U}. \quad (5)$$

where $\overset{\leftrightarrow}{\alpha}$ denotes the (complex) excess polarisability tensor of the NP, where the tensorial nature of the polarisability can derive from either an optical anisotropy of the NP (i.e. via $\overset{\leftrightarrow}{\epsilon}_p$)

or through shape anisotropy (which is of more interest for our case) [4]. U can be interpreted as the total energy initially stored in the WGM, whilst $\text{Re}[\Delta U] \approx \text{Re}[\int_{V_p} \mathbf{E}^\dagger(\mathbf{r})\mathbf{P}(\mathbf{r})d\mathbf{r}]/2$ is the energy used to polarise the NP. It should be noted that derivation of Eq. (5) is done in the quasi-static limit, such that the NP is assumed to experience a uniform field $\mathbf{E}(\mathbf{r}_p)$.

In addition to absorption losses described by Eq. (3), the presence of a NP also introduces scattering losses from the WGMR, which have not yet been accounted. When multiple broadening mechanisms, such as curvature (radiation) losses, scattering losses, and heating losses etc, are present

$$Q^{-1} = Q_{\text{rad}}^{-1} + Q_{\text{abs}}^{-1} + Q_{\text{sca}}^{-1} + \dots \quad (6)$$

or equivalently $\gamma = \gamma_0 + \Delta\gamma_{\text{abs}} + \Delta\gamma_{\text{sca}} + \dots$. To determine the scattering losses we can again consider the NP as a dipole scatterer, with induced dipole moment $\mathbf{P}_T = \int_{V_p} \mathbf{P}(\mathbf{r})d\mathbf{r}$. We further recall the definition of the quality factor of a resonance viz.

$$Q = \omega_0 \frac{\text{Energy stored}}{\text{Power loss (per second)}} = \omega_0 \frac{U}{P} \quad (7)$$

Under our approximation of a dipole scatterer we can assert that the power scattered is given by the well known Larmour's formula viz.

$$P = \frac{n_h \omega_0^4 |\mathbf{P}_T|^2}{12\pi \epsilon_0 c^3} = \frac{n_h^5 \omega_0^4 \epsilon_0}{12\pi c^3} |\hat{\alpha} \mathbf{E}(\mathbf{r}_p)|^2 \quad (8)$$

where n_h is the refractive index of the immersion medium, hence yielding

$$\Delta\gamma_{\text{sca}} = \frac{n_h^5 \omega_0^4 \epsilon_0}{12\pi c^3} \frac{|\hat{\alpha} \mathbf{E}(\mathbf{r}_p)|^2}{U}. \quad (9)$$

It should be noted that this classical derivation is consistent with a more rigorous quantum treatment [9]. Finally, an additional loss term $\Delta\gamma_{\text{cc}}$ term should also be included, if the coupling strength is greater than the damping rate of the resonator i.e $\omega_0/Q_0 < 2\Delta\omega$. In this regime, scattering from a particle bound to the microresonator couples light appreciably into a (initially degenerate) counter-propagating WGM [10], such that the amplitude of the original and counter-propagating WGM are roughly equal. When the particle induced splitting ($= 2\Delta\omega$) of the two resulting standing wave eigenmodes of the resonator, is $\sim \omega_0/Q_0$ the splitting can not be resolved, but gives rise to an apparent broadening $\Delta\gamma_{\text{cc}}$ [11]. Naturally, when $\omega_0/Q_0 \ll 2\Delta\omega$ mode splitting is observed [9, 12].

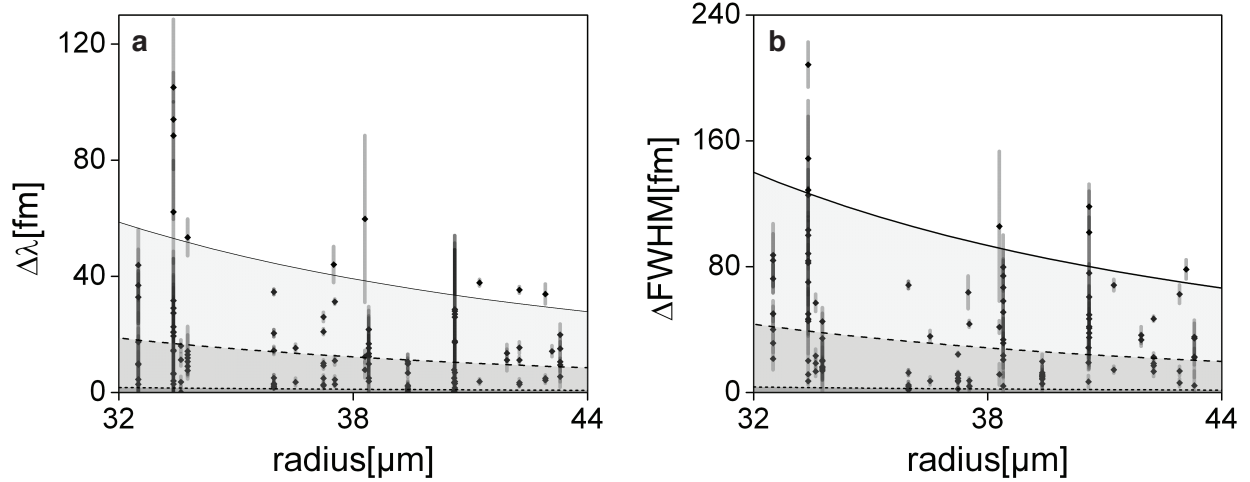
2. Plasmonic nanorod

We consider first the perturbation induced by a gold nanorod of dimensions $L = 42$ nm and $D = 12$ nm and deduce the theoretical maximum resonance shift and linewidth change to a WGM with resonance wavelength ~ 780 nm. To maximise observable resonance shifts we assume that the NP binds on the equatorial plane of the microsphere and binds such that its orientation is parallel to the mode polarisation. This arrangement ensures the WGM couples only to the longitudinal plasmon resonance in the NP. To determine the polarisability of the nanorod, Waterman's extended boundary condition method (also known as the null field method) was used to determine the T -matrix of the particle. The longitudinal dipole contribution, $T_{1,0}^E$, can then be extracted and used to determine the longitudinal polarisability of the NP according to

$$\alpha_{1,0} = -4\pi \frac{3i}{2k^3 n_h^3} T_{1,0}^E \quad (10)$$

where $k = 2\pi/\lambda = \omega c$. T -matrix calculations were verified by calculating the scattering spectrum of an isolated nanorod as a function of incident wavelength, yielding a resonance frequency of ~ 740 nm. The calculated scattering spectrum was compared with that calculated in COMSOL Multiphysics for a plane wave incident upon a nanorod in water and found to be in good agreement. Furthermore, the determined resonance wavelength was found to be in agreement with that quoted (756 nm) on the nanorod data sheet supplied by the manufacturers. As a slight digression, it should be noted, that by use of the polarisability of Eq. (10), Eq. (5) (and subsequent) are valid beyond the quasi-static limit, since the polarisability derived from the T -matrix accounts fully for retardation effects across the particle. Noting further that if we adopt the position of the scatterer \mathbf{r}_p as the origin of a new coordinate frame, in which the incident field is decomposed into a multipolar basis, the only non-zero contribution at the NP position is the electric dipole mode [13]. The field strength $\mathbf{E}(\mathbf{r}_p)$ therefore corresponds to the electric dipole mode of the illumination field in the shifted coordinate system. We can thus conclude that Eq. (5) (and subsequent) are valid within a dipole approximation and is thus valid for scattering from NPs exhibiting strong electric dipole resonances.

Determination of the maximum shift and linewidth broadening also requires solution of the well-known resonance condition for spherical cavities [4]. Solutions were found using root finding algorithms seeded with asymptotic solutions for high order Mie modes [14]. Mode



Supplementary Figure 4. Step heights for nanorod bindings extracted from **a.** $\Delta\lambda$ and **b.** ΔFWHM traces of TE polarized WGMs excited in microspheres with different radius. Lines are theoretical predictions, taking into account a possible angle of the nanorods long axis with respect to the microcavity surface of $\sim 0^\circ$ (solid line), $\sim 30^\circ$ and $\sim 90^\circ$ (dashed lines).

profiles and energy were then calculated using standard expressions for the Mie modes (see. e.g. [6]) and substituted into the perturbative equations detailed above. The results of this calculation are shown in Figure 2 of the main text for TM modes. Similar calculations were also performed for TE modes and are shown in Supplementary Figure 4. Importantly, TM WGM modes have non-zero field vectors in both the radial and azimuthal direction. Consequently, assuming the particle binds with its long axis parallel to the microsphere surface it is not possible to fully couple to the longitudinal resonance. The full tensorial polarisability, which in the nanorod's principle frame of reference was calculated to be

$$\vec{\alpha} = \begin{pmatrix} 1.143 + 0.01495i & 0 & 0 \\ 0 & 1.143 + 0.01495i & 0 \\ 0 & 0 & 27.58 + i10.64 \end{pmatrix} \times 10^{-23} \text{ m}^3, \quad (11)$$

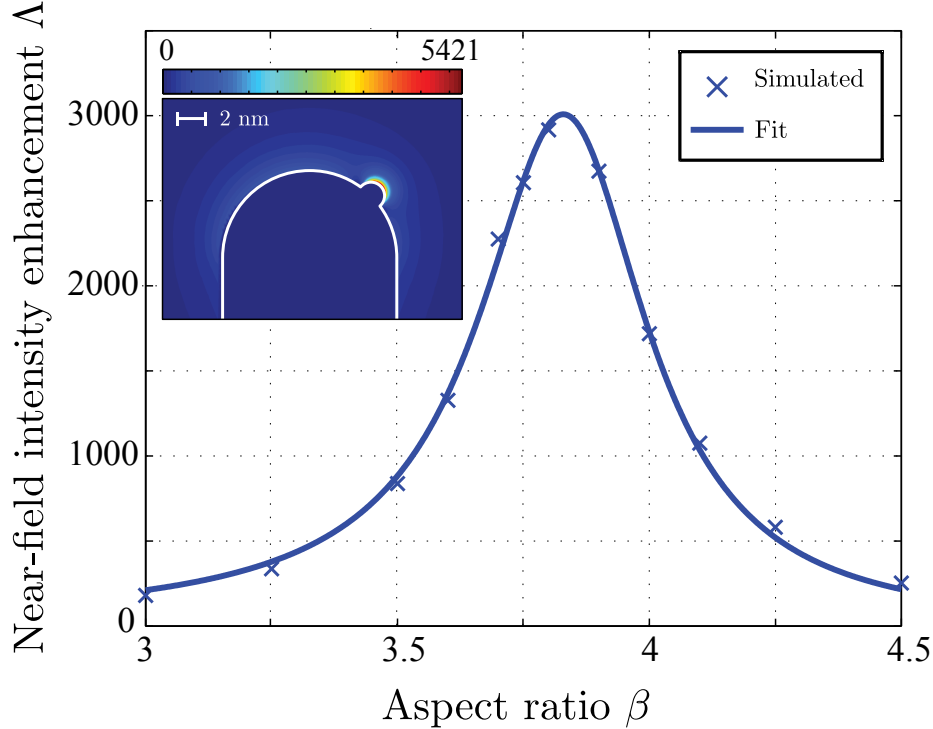
must then be used in Eq. (5). Resonance shifts for different nanorod binding angles can be determined by applying a suitable tensor rotation to the polarisability [6].

3. DNA strands

We now consider the resonance shift induced by a DNA strand. In particular we consider a strand of 22 bases, each of which is of dimension $3.4 \text{ \AA} \times 10 \text{ \AA}$. To model a single strand we adopt the Rayleigh-Gans approximation and consider it as a dielectric prolate ellipsoid of refractive index $n_p = 1.5$ of total length 3.74 nm and diameter 1 nm. To calculate the induced resonance shift we consider Eq. (5), however we now assume that the local intensity has been enhanced by a factor Λ and further assume the long axis of the dielectric DNA ellipsoid to lie parallel to the local field, such that

$$\frac{\Delta\omega_{\text{DNA}}}{\text{Re}[\alpha_{1,0}^{\text{DNA}}]} = \Lambda \frac{\Delta\omega_{\text{NP}}}{\text{Re}[\alpha_{1,0}^{\text{NP}}]} \quad (12)$$

in the best case scenario (and similarly for line broadening). In reality, it should be noted that due to the finite extent of a bound biomolecule, Λ in Eq. (12) would represent an effective near field enhancement determined from the ratio of the integrated intensities (over the volume of the biomolecule) with and without the nanorod integrated. Given the small size of a single DNA strand, we neglect this effect and assume the binding position \mathbf{r}_p lies within the maximum of the plasmonic hotspot. The unenhanced resonance shift at this position for a microsphere of radius $30 \mu\text{m}$ and TE WGM of order $l = 340$ were calculated as $\approx 0.00025 \text{ fm}$. Again the line broadening upon binding of a DNA to the nanorod can also be determined, albeit here we note that $\omega_0/Q_0 \gg 2\Delta\omega$, such that we may neglect the $\Delta\gamma_{\text{cc}}$ term, yielding negligible broadening. Assuming an enhancement factor of $\Lambda \approx 800$, as determined from the full near field calculations described above, ultimately yields a maximum expected resonance shift of 0.2 fm. This is smaller than those observed experimentally by approximately one to two orders of magnitude. This discrepancy is attributed to two main factors. Firstly, size dispersion of the nanorods implies that the plasmonic resonance of each binding nanorod lies at a different wavelength. The relative detuning of each plasmonic nanorod with respect to the WGM in turn varies such that the local near field intensity enhancement achievable differs between each bound particle. To quantify this effect, the aspect ratio of the nanorod was varied in a series of COMSOL simulations (see above) and the maximum intensity enhancement for each case was determined. The results are shown in Supplementary Figure 5 by the cross markers. The solid blue line in Supplementary Figure 5 depicts a numerical fit of the experimental data adopting the lineshape given in the work of Zuloaga and Nordlander



Supplementary Figure 5. Calculated near field intensity enhancement for a nanorod placed 7 nm from a WGM resonator as a function of nanorod aspect ratio L/D . Inset shows intensity enhancements in the vicinity of a nanorod (of aspect ratio $L/D = 3.5$) with a 1 nm radius spherical protrusion. White solid line depicts the surface of the nanorod.

[15]. It can be seen that for aspect ratios of ~ 3.8 , an enhancement of ~ 3000 can be achieved.

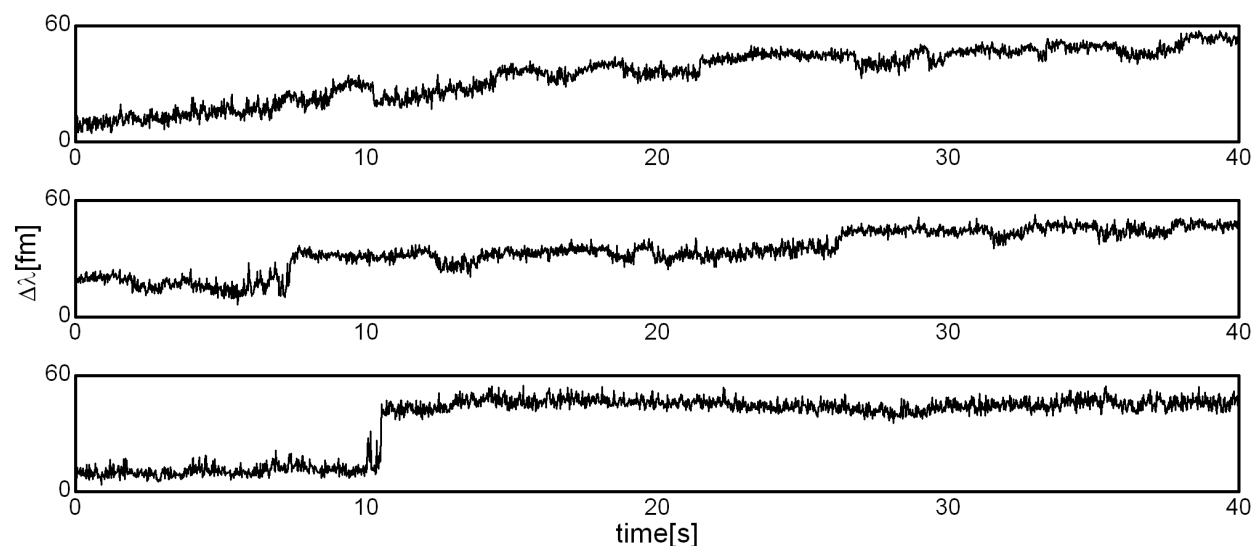
Secondly, in the work of Dantham et al. [16] surface roughness was demonstrated to give rise to large discrepancies between theoretical predictions and experimental results. Similar effects are also believed to play a role in our case, since some degree of surface roughness is unavoidable given current day fabrication techniques. To quantify the additional enhancements arising as a consequence of roughness, we introduce a small 1 nm radius protrusion to the surface of the nanorod in a similar vein to [16]. For a nanorod of aspect ratio 3.5, a local intensity enhancement of over 5400 fold is seen observed as shown in the inset of Supplementary Figure 5. In combination it is thus seen that both surface roughness and nanoparticle size dispersion can easily account for the discrepancy described above.

SUPPLEMENTARY INFORMATION 3. THIOL REACTION

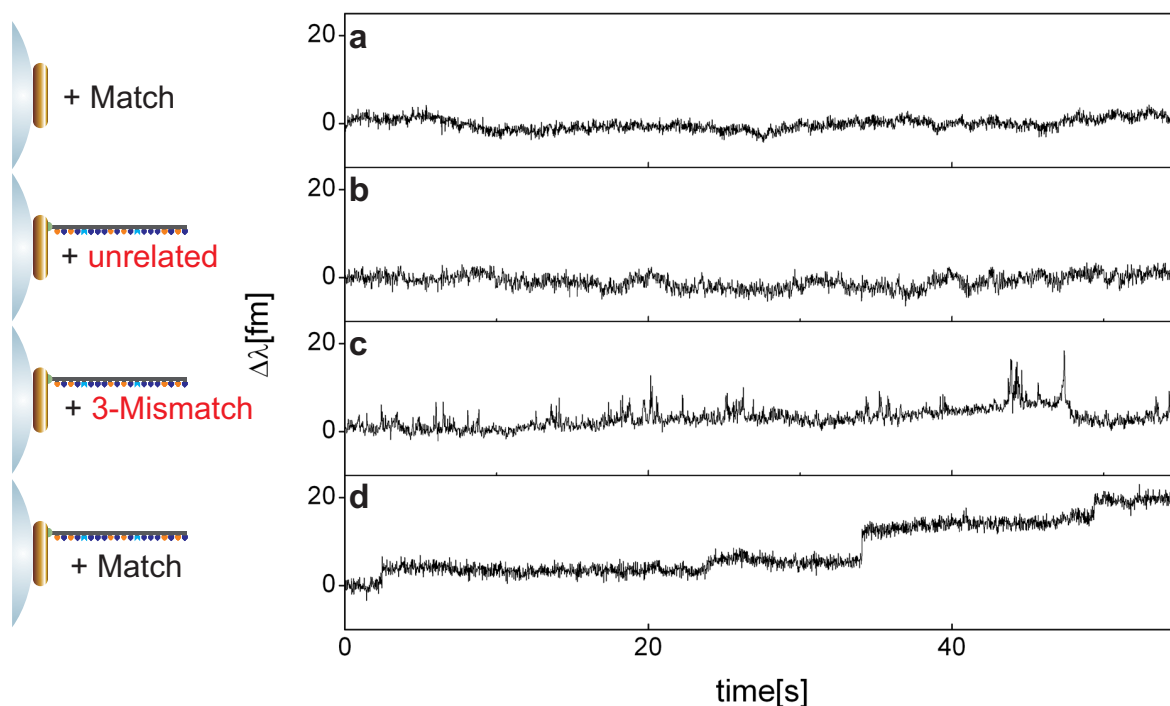
The thiol reactions are performed in ultrapure distilled water, filtered with 0.1 μm membrane filters, pH is adjusted with HCl to pH ~ 3 , 0.5 M NaCl, 0.02 % w/w SDS. Reaction time is on the order of 10 to 30 minutes. A representative trace of WGM shift $\Delta\lambda$ during the thiol reaction is shown in Supplementary Figure 6. In addition to binding and unbinding steps we observe large random fluctuations which we attribute to rapid exchange of CTAB and SDS molecules at the nanorod surface. Without SDS, conditions for which the yield of the thiol reaction drops significantly, these random fluctuations are no longer seen.

SUPPLEMENTARY INFORMATION 4. NUCLEIC ACIDS INTERACTIONS CONTROL EXPERIMENTS

Supplementary Figure 7a shows a WGM $\Delta\lambda$ trace after addition of ~ 100 nM oligonucleotide (22 mer, 10 mM NaCl, pH 7) without modification of the nanorod with a receptor oligonucleotide. No signals are observed indicating the absence of detectable unspecific inter-



Supplementary Figure 6. Thiol reaction with gold nanorods. In addition to binding and unbinding steps due to the reaction of a thiol modified oligonucleotide we record random fluctuations in the WGM wavelength trace $\Delta\lambda$, indicating rapid exchange of SDS and CTAB molecules at the nanorod surface. The three WGM traces show progression of the thiol reaction.

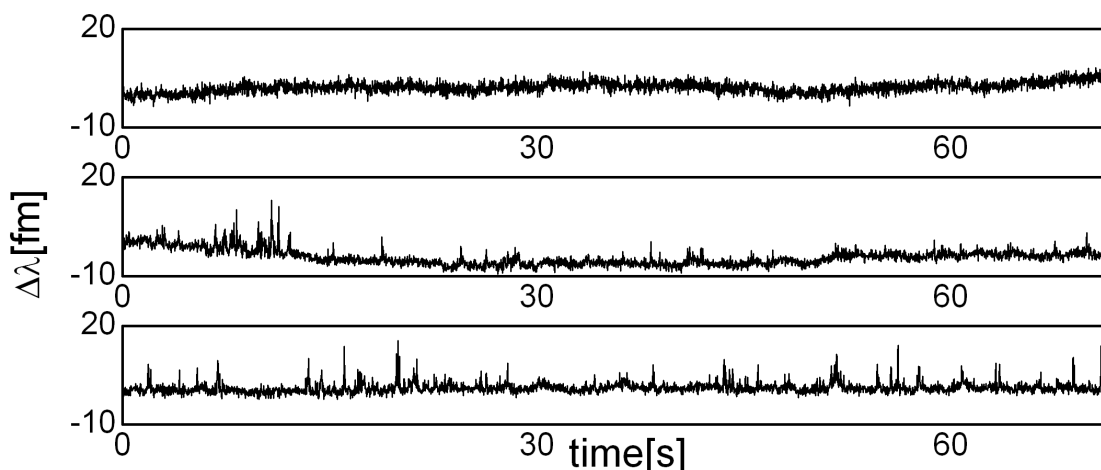


Supplementary Figure 7. Control experiments, all concentrations ~ 100 nM. **a.** No significant WGM $\Delta\lambda$ shift signals are observed for a non-functionalized nanorod. **b.** No significant WGM shifts are observed for interaction of a 22 mer oligonucleotide receptor with an unrelated oligonucleotide. **c.** Characteristic spikes of the WGM signal for interaction of the receptor with a 3 base mismatched strand. **d.** WGM $\Delta\lambda$ shifts recorded for a 22 mer oligonucleotide receptor interacting with its matching strand. Steps indicate hybridization.

actions between nucleic acids and the non-functionalized gold rod. Supplementary Figure 7b shows that no significant WGM shift signals are observed for an unrelated oligonucleotide. For this experiment, the nanorod was modified with 22 mer oligonucleotide receptors and the unrelated oligonucleotide was added to final concentration ~ 100 nM. Spikes in the WGM $\Delta\lambda$ trace appear only after adding a 3 base mismatched oligonucleotide at the same concentration, as shown in Supplementary Figure 7c. The spikes indicate a transient interaction between the receptor with its 3 base mismatched strand; similar data is shown in Figure 3 of the main manuscript. Supplementary Figure 7d shows result from a hybridization experiment. This WGM $\Delta\lambda$ trace shows the 22 mer receptor interacting with its complementary

matching strand. Steps in the WGM signal indicate hybridization. Unbinding of the complementary oligonucleotide from the receptor was not observed, indicating a very low off rate for a 22 mer oligonucleotide under these experimental conditions (pH 7, 10 mM NaCl, $\sim 20^\circ\text{C}$).

SUPPLEMENTARY INFORMATION 5. CONCENTRATION DEPENDENCE FOR DISCRIMINATING SINGLE BASE MISMATCH WITH A SHORT RECEPTOR

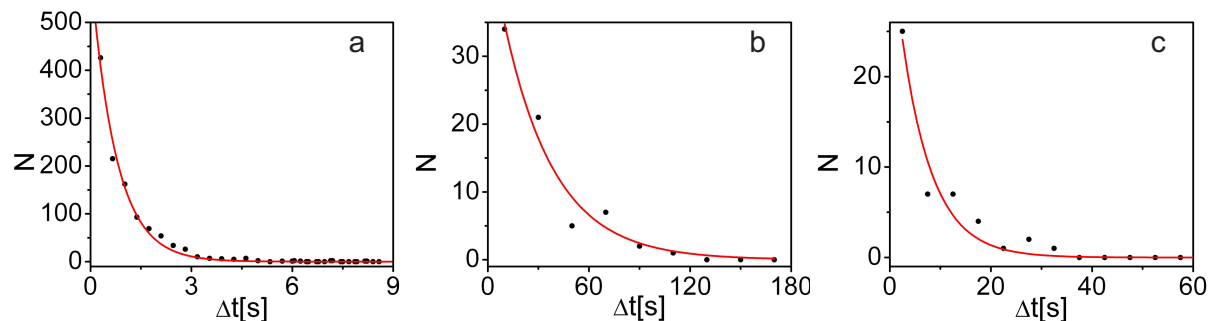


Supplementary Figure 8. Top trace: no WGM signals are observed for interaction of the 16 mer oligonucleotide receptor with a single base mismatched strand at 20 mM NaCl. Middle trace: Measurements with the matching strand (~ 120 nM) show spikes in the WGM signals at 20 mM NaCl. Bottom trace: More spikes appear after increasing the matching strand concentration by 5 fold to final concentration ~ 0.8 μM .

SUPPLEMENTARY INFORMATION 6. POISSONIAN STATISTICS OF SINGLE MOLECULE INTERACTION EVENTS

The Poisson distribution is a discrete probability distribution describing the probability of observing N “rare” events of interest within a fixed time interval. Underlying the Poisson distribution is the assumptions that within a given infinitesimal time interval the probability of two events occurring is negligible, with only one or zero events being possible, in addition

to the assumption of statistical independence of event occurrences between non-overlapping time intervals [17]. Closely related to the Poisson distribution for the number of observed events (in our case binding or transient events) is the exponential distribution, which describes the the statistics of the waiting time between events obeying Poisson statistics. To verify the single molecule nature of our observed events [18], we have thus performed a statistical analysis on the time intervals between observed interaction events (see Supplementary Figure 9), in which we find very close agreement with the expected exponential statistics for single molecule events. The graphs shown in Supplementary Figure 9 are typical of fits performed on our datasets.



Supplementary Figure 9. Statistics on time intervals between observed interaction events for a) three base pair mismatched oligonucleotide at 500 nM concentration interacting with a 22 mer receptor: exponential decay const = $0.75 \text{ s} \pm 0.03 \text{ s}$, R^2 of exponential fit is 0.989. b) binding events for octamer at 285 nM concentration: exponential decay const = $30 \text{ s} \pm 3.5 \text{ s}$, $R^2 = 0.966$, and c) intercalating small molecules at 250 pM concentration: decay const = $6.1 \text{ s} \pm 0.6 \text{ s}$, $R^2 = 0.956$.

Given the measured decay constants τ_c it is possible to calculate the expected number of events between subsequent data points in our time trace, i.e. within our time resolution of $\tau_m = 20 \text{ ms}$ according to the Poisson distribution

$$p(n) = \frac{(\mathcal{R}\tau_m)^n}{n!} \exp[-\mathcal{R}\tau] \quad (13)$$

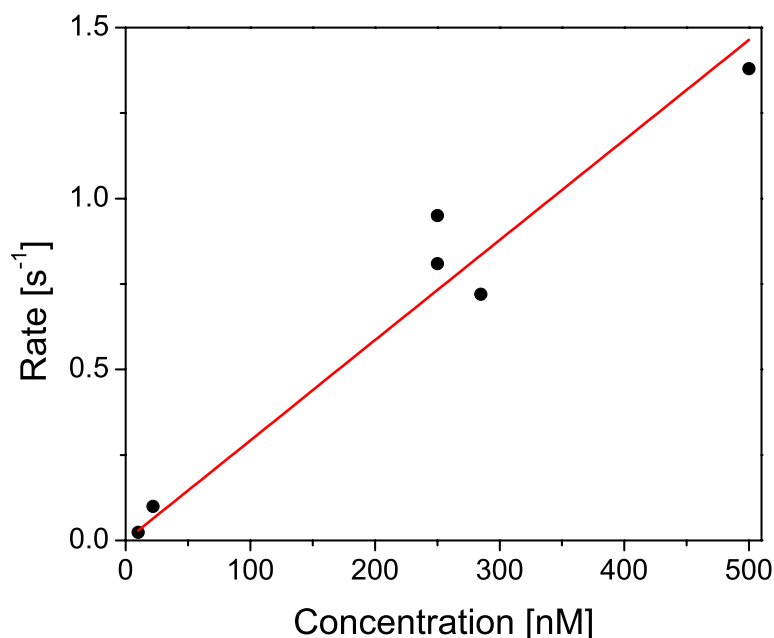
where $\mathcal{R} = 1/\tau_c$ is the event rate. The calculated probabilities for one, two and three events for each of the cases depicted in Supplementary Figure 9 are shown in Supplementary Table 2. The likelihood of multiple events within our time resolution is evidently very low, relative to the probability of a single event.

n	Supp. Fig. 9a)	Supp. Fig. 9b)	Supp. Fig. 9c)
1	0.0260	0.000666	0.00326
2	0.000346	2.22×10^{-7}	5.36×10^{-6}
3	3.08×10^{-6}	4.93×10^{-11}	5.85×10^{-9}

Supplementary Table 2. Calculated probabilities of multiple events within a 20 ms time window, for the cases shown in Supplementary Figure 9.

SUPPLEMENTARY INFORMATION 7. CONCENTRATION SCALING OF EVENT RATE

Experiments were also performed to investigate the concentration dependence of observed transient events. We have determined the average rate \mathcal{R} directly from the time trace of wavelength shift measurements (see Supplementary Information 6) by determining the average rate of spike events due to single molecular interactions of a three mismatched



Supplementary Figure 10. Concentration dependence of average rate of spike events for a 3 base mismatched 22 mer single strand DNA. Slope of linear fit = $2.93 \times 10^6 \text{ M}^{-1}\text{s}^{-1}$ ($R^2 = 0.977$).

single DNA strand. In each case the number of bound nanorods is the same and hence the number of receptors is comparable. The determined rate increases linearly with the DNA concentration as shown in Supplementary Figure 10, as would be expected for single molecule events. Specificity of the signal follows since the unrelated DNA sequence does not produce any significant signal (spike events) in control experiments. Linear fitting of the data yields a slope of $2.93 \times 10^6 \text{ M}^{-1}\text{s}^{-1}$ ($R^2 = 0.977$), such that, considering an average of 20 receptors (as determined from counting subsequent binding events observed upon change of salt concentration), we can extract an average kinetic on-rate k_{on} for this 3 base mismatched 22 mer of $k_{\text{on}} = 1.47 \times 10^5 \text{ M}^{-1}\text{s}^{-1}$. This value is in agreement with published values of similar experiments for which on-rates of $k_{\text{on}} \sim 10^5\text{--}10^6 \text{ M}^{-1}\text{s}^{-1}$ are reported [19–22].

-
- [1] Kaplan, A. *et al.*, Finite element simulation of a perturbed axial-symmetric whispering-gallery mode and its use for intensity enhancement with a nanoparticle coupled to a microtoroid. *Opt. Express* **21**, 14169–14180 (2013).
 - [2] Palik, E.D. *Handbook of Optical Constants of Solids*, (Academic Press, Boston, 1985).
 - [3] Berenger, J.-P. A perfectly matched layer for the absorption of electromagnetic waves. *J. Comput. Phys.* **114**, 185–200 (1994).
 - [4] Bohren, C.F. and Huffman, D.R. *Absorption and scattering of light by small particles* (John Wiley & Sons, Inc, Weinheim 1998).
 - [5] Hale, G.M. and Querry, M.R. Optical Constants of Water in the 200-nm to 200- μm Wavelength Region. *Appl. Opt.* **12**, 555–563 (1973).
 - [6] Foreman, M.R. and Vollmer, F. Theory of resonance shifts of whispering gallery modes by arbitrary plasmonic nanoparticles. *New J. Phys.* **15**, 083006 (2013).
 - [7] Teraoka, I. and Arnold, S. Theory of resonance shifts in TE and TM whispering gallery modes by nonradial perturbations for sensing applications. *J. Opt. Soc. Am. B* **23**, 1381–1389 (2006).
 - [8] Arnold, S., Ramjit, R., Keng, D., Kolchenko V. and I. Teraoka MicroParticle photophysics illuminates viral bio-sensing. *Faraday Discuss.* **137**, 65–83 (2008).
 - [9] Zhu, J. *et al.* On-chip single nanoparticle detection and sizing by mode splitting in an ultrahigh- Q microresonator. *Nat. Photonics* **4**, 46–49 (2010).

- [10] Weiss, D.S. *et al.* Splitting of high-Q Mie modes induced by light backscattering in silica microspheres. *Opt. Lett.* **20**, 1835–1837 (1995).
- [11] Shao, L. *et al.* Detection of Single Nanoparticles and Lentiviruses Using Microcavity Resonance Broadening. *Adv. Mat.* **25**, 5616–5620 (2013).
- [12] Yi, X. *et al.* Mode-splitting-based optical label-free biosensing with a biorecognition-covered microcavity. *J. Appl. Phys.* **111**, 114702 (2012).
- [13] Foreman, M.R., Sivan, Y., Maier, S.A. and Török, P. Independence of plasmonic near-field enhancements to illumination beam profile *Phys. Rev. B* **86**, 155441 (2012).
- [14] Schiller, S. Asymptotic expansion of morphological resonance frequencies in Mie scattering. *Appl. Opt.* **32**, 2181–2185 (1993).
- [15] Zuloaga, J. and Nordlander, P. On the energy shift between near-field and far-field peak intensities in localized plasmon systems. *Nano. Lett.* **11**, 1280–1283 (2011).
- [16] Dantham, V.R. *et al.* Label-free detection of single protein using a nanoplasmonic-photonic hybrid microcavity. *Nano. Lett.* **13**, 3347–3351 (2013).
- [17] Goodman, J.W. *Statistical Optics* (John Wiley & Sons, Ltd., New York, 2000).
- [18] Armani, A.M., Kulkarni, R.P., Fraser, S.E., Flagan, R.C. and Vahala, K.J. Label-free, single-molecule detection with optical microcavities. *Science* **317**, 783–787 (2007).
- [19] Jungmann, R. *et al.* Single-molecule kinetics and super-resolution microscopy by fluorescence imaging of transient binding on DNA origami. *Nano Lett.* **10**, 4756–4761 (2010).
- [20] Hannestad, J.K. *et al.* Kinetics of diffusion-mediated DNA hybridization in lipid monolayer films determined by single-molecule fluorescence spectroscopy. *ACS Nano.* **7**, 308–315 (2013).
- [21] McCauley, M.J., Rueter, E.M., Rouzina, I., Maher III, L.J. and Williams, M.C. Single-molecule kinetics reveal microscopic mechanism by which High-Mobility Group B proteins alter DNA flexibility. *Nuc. Acid. Res.* **41**, 167–181 (2013).
- [22] Long, F., Wu, S., He, M., Tong, T. and Shi, H. Ultrasensitive quantum dots-based DNA detection and hybridization kinetics analysis with evanescent wave biosensing platform. *Biosens. Bioelec.* **26**, 2390–2395 (2011).